PEER REVIEWED

Size Effects of Brittle Particles in Aerosol Deposition—Molecular Dynamics Simulation

Bahman Daneshian[1] · Frank Gaertner[1] · Hamid Assadi[2] · Daniel Hoeche[3] · Wolfgang Weber[1] · Thomas Klassen[1,3]

Abstract Up to now, the role of particle sizes on the impact behavior of ceramic particles in aerosol deposition not yet fully understood. Hence, with the aim to supply a more general understanding, modeling series of low strain rate compression and high-speed impact were performed by molecular dynamics on single-crystalline particles in sizes of 10-300 nm that are tuned to match mechanical properties of TiO_2-anatase. The modeling results reveal that particles with original diameter of 25-75 nm exhibit three different impact behaviors that could be distinguished as (i) rebounding, (ii) bonding and (iii) fragmentation, depending on their initial impact velocity. In contrast, particles larger than 75 nm do not exhibit the bonding behavior. Detailed stress and strain field distributions reveal that combination of "localized inelastic deformation" along the slip systems and "shear localization" cause bonding of the small and large particles to the substrate. The analyses of associated temperature rise by the inelastic deformation revealed that heat diffusion at these small scales depend on size. Whereas small particles could reach a rather homogeneous temperature distribution, the evolved heat in the larger ones keeps rather localized to areas of highest deformation and may support deformation and the formation of dense layers in aerosol deposition.

Keywords aerosol deposition · molecular dynamics · nanoparticle · size effect · TiO_2

Abbreviations
AD   Aerosol deposition
CS   Cold spraying
MD   Molecular dynamics
2-D   Two-dimensional

Symbols
r Interatomic distance in Lennard-Jones potential function, Å (= 0.1 nm)
r_c Cutoff distance in Lennard-Jones potential function, Å (= 0.1 nm)
U Lennard-Jones potential energy, eV
v_P Particle velocity, ms^{-1}
ε Lennard-Jones energy parameter, eV
σ Lennard-Jones characteristic length parameter, Å (= 0.1 nm)

✉ Bahman Daneshian
bahman.daneshian@hzg.de

[1] Helmut Schmidt University/University of the Federal Armed Forces Hamburg, Holstenhofweg 85, 22043 Hamburg, Germany

[2] Brunel Centre for Advanced Solidification Technology (BCAST), Brunel University London, Kingston Ln, Greater London, Uxbridge UB8 3PH, UK

[3] Center for Materials and Coastal Research GmbH, Helmholtz-Zentrum Geesthacht, Max-Planck Straße 1, 21502 Geesthacht, Germany

Introduction

Aerosol deposition (AD) is a room-temperature spraying technique for producing ceramic films on a variety of substrate materials, including metals, ceramics and even

polymers (Ref 1-5). By this method, submicron to micron size ceramic particles (Ref 1-5) are accelerated to velocities of typically 100-550 m/s by a gas flow through a converging nozzle and expansion into a vacuum chamber, where they impact onto the substrate (Ref 1-5). With respect to high-velocity solid-state impacts, AD has some similarity to cold spraying (CS), which is usually applied for the deposition of ductile materials (Ref 6). For CS, bonding mechanisms are associated with adiabatic shear instabilities (ASI) (Ref 7). In AD, however, particles are brittle and lack the plastic deformability that is needed to reach conditions for adiabatic shear instability. Therefore, bonding mechanisms in AD must be different from those of CS. So far, three different hypotheses like room temperature impact consolidation (RTIC) (Ref 3, 8, 9), fragmentation and packing consolidation (Ref 10) and bonding between newly formed fractured surfaces (Ref 11) have been presented as possible bonding mechanisms of brittle particles in AD. Nevertheless, no common model concerning bonding mechanism has yet been approved; some of the discussed hypotheses are even controversial. Thus, there is a need for systematic investigations, particularly modeling, to reach a better understanding of the bonding mechanisms in AD. Associated models should address open questions concerning the roles of (i) ceramic particle sizes, (ii) their impact velocities and (iii) the observed nano-crystallization in deposited layers (Ref 1-3). This study mainly focuses on the first two questions.

One fundamental aspect of AD is that bonding is successful only for small particles, of typically submicron to several micron sizes (Ref 1-5, 12), thus dealing with much smaller dimensions than used in CS (Ref 6). There are few reports on CS of ceramics, but they mainly deal with loose agglomerates of submicron primary ceramic particles; thus, basic mechanisms may be similar to those of AD (Ref 13). For successful coating formation by AD, particle sizes need to be small, but not too small. Certain critical minimum and maximum sizes can be deduced from experiments (Ref 14-16). Whereas the lower limit can be attributed to (i) the fluid dynamics of fine particles and deceleration by the bow shock in front of the substrate (Ref 14) and (ii) needed grain refinement in AD (Ref 17, 18), reasons for the definition of the upper limit are not yet clear. Concerning the former point for minimum sizes (i), fluid dynamic simulations confirmed that very fine particles do not reach to the substrate by changing their flight direction along with the gas flow in front of the substrate (Ref 14). Respectively, needed inertias define a minimum size of the ceramic particles for reaching the substrate with sufficiently high velocity for successful deposition of dense ceramic layers via AD. Concerning the later point for minimum sizes (ii), experimental observations identified a sufficiently effective grain refinement as necessary prerequisite for layer

formation by AD (Ref 17, 19, 20). So far, it is still under discussion whether this grain refinement is just needed for geometrical rearrangement to form dense layers from originally more equiaxed particles or whether fresh surfaces of nano-fragments could play a role (Ref 11). The upper limit of suitable particle sizes is mainly a matter of achievable impact velocities, being lower for larger particles by their high inertia (Ref 18).

The experimental results regarding needed particle sizes in AD and process conditions are very case sensitive. For example, experimental studies for the case of alpha-Alumina (Ref 2, 3, 15) report that particles with the typical size of 100-700 nm create dense AD coating layers. Too fine alpha-Alumina particles change direction during spraying not contributing to the formation of AD layers. In contrast, alpha-Alumina particles larger than 700 nm do not form dense AD layers and they rather cause surface erosion effects on the substrate like regular sandblasting. In case of TiO_2-anatase powders, the larger particles of up to sizes 2.4 micron could be successfully deposited via AD (Ref 19, 20). However, so far no minimum size limit for the deposition of TiO_2-anatase powders has been reported yet. Since most of currently reported data deal with rather similar process conditions used for AD, respective in needed size ranges for successful layer formation of different materials might be attributed to individual deformation and grain refinement features depending on material properties.

Furthermore, it should also be mentioned that, despite the influence of the particle size alone, there are also several evidences that the initial condition of powders like humidity (Ref 5) and powder preparation methods like ball milling (Ref 5) can greatly influence the performance in layer formation by AD. In addition, studies showed that particles of submicron to micron size are strongly prone to agglomeration either by electrostatic surfaces charges or van der Waals interactions that could hinder deposition (Ref 5). Although agglomeration can be reduced by application of the vibration of the powder generator, re-agglomeration of small particles may be again happened during the fluidized flow (Ref 5). Therefore, it is rather challenging to derive respective correlations or distinctions between possible influences of powder conditions and treatment on the success of layer formation in AD.

So far, the experimental results regarding needed particle sizes for AD give guidelines for layer formation, but by the complexity of influences still miss explanations for deriving general rules. Computer modeling has the advantage that it allows to focus on individual questions and influential parameters, and step-by-step making models more complex to adopt to realistic conditions.

Despite ceramic materials usually behaving brittle, it has so far been well established that cracking in ceramics under

compression can be suppressed at small length scales (Ref 21, 22). Recent studies reveal that submicron ceramics like Al_2O_3 nanoparticles (Ref 23, 24), TiO_2-anatase nanoparticles (Ref 25), MgO nanocubes (Ref 26), GaAs micropilars (Ref 27) and silicon nanoparticles (Ref 28) show ductility and plastic deformation under quasi-static compression at room temperature. These results can be explained by a brittle to ductile transition occurring at small scales. However, in a spraying process like AD, also the high deformation rates of ceramic particles have to be taken in account.

The aim of this study is to shed some light onto the influence of size of monolithic or even single-crystalline brittle particles on their deposition behavior in AD by series of molecular dynamic (MD) computations (Ref 29). With respect to potential applications of AD coatings in photo-catalysis and water splitting for hydrogen production, TiO_2-anatase has been selected as model system (Ref 30). To mimic the deformation of TiO_2-anatase during impact in AD, respective mechanical properties were separately adjusted in the model system. The molecular dynamics method (MD) was selected because of its ability for detailed analysis of field variables such as stress, strain and temperature at small length scales for fast phenomena like the AD impact processes. In addition, MD is in principle capable even to monitor nanocrystallization, a feature being relevant for AD coating formation (Ref 1-5). In comparison with previous MD analysis and other computer modeling attempts of AD (Ref 3, 8, 9, 31, 32), where only few and mainly very small sizes were studied, the present study covers a significantly wider range and particularly larger particle sizes of up to 300 nm. In addition, extracting local field variables like atomic stress, atomic strain and local temperature, the present study allows for providing details on the impact behavior and associated deformation mechanism. By the lack of suitable analytical methods in MD, such was not possible at the time when previously reported results were created (Ref 8, 31, 32).

In the present case, a two-dimensional (2-D) MD approach was applied in order to reduce the computational time. The applied series of MD modeling should supply detailed information on stress, strain and temperature distribution to contribute to the understanding of the impact process and bonding mechanism in AD.

Modeling Methods

In this study, 2-D MD simulations of slow rate compression and high-speed particle impact were performed for single-crystalline particles in order to cover a wide size regime ranging up to sizes of 300 nm. Although original sizes of particles in AD are typically in a submicron to some micron range (Ref 5), maximum particle diameters had to be limited to 300 nm due to limitation of MD with respect to needed computational times. Instead of using long-range Coulombic interactions between ions inside the anatase structure, which could drastically increase simulation efforts for large particles, a modified Lennard-Jones potential was applied to mimic the mechanical properties of TiO_2-anatase as given in Eq 1, in order for keeping computational times in acceptable ranges:

$$U = \varepsilon\left[\left(\frac{\sigma}{r}\right)^{12} - \left(\frac{\sigma}{r}\right)^6\right], r < r_c = 3.345\ \text{Å (1)} \tag{1}$$

where r is the distance between two atoms and r_c is an adjustable cutoff radius. $\sigma = 2.23$ Å is characteristic length scale and ε is the energy parameter. Brittleness was introduced by adjusting the cutoff distance of the attractive potential. The ε parameter was tuned by tensile and compression MD simulations in order to mimic the brittleness, Young's modulus and the compression behavior of a 33-nm single-crystal TiO_2-anatase particle for matching the compressive strength reported in the literature (Ref 25, 33). By applying rather slow deformation rates in single-particle compression, the modified Lennard-Jones potential function was adjusted to reproduce the experimentally observed deformation data with respect to similar compressive strength and Young's modulus. The tuned potential function was then applied for following simulations of tensile tests, the deformation of TiO_2 particles of various sizes in compression and the impact behavior in AD. By subsequent fine-tuning, r_c and the ε parameter in Eq 1 were set to 3.345 Å and 0.45 eV, respectively. The 2-D tensile test model was cut from a large single crystal with closed-packed atomic structure, i.e., a (11) plane in 2-D. Figure 1 shows the tensile test model setup (Fig. 1a), the brittle failure configuration in the cross section of the model after simulation (Fig. 1b) and the computed stress–strain diagram (Fig. 1c), demonstrating the brittle behavior of the model material.

It should be noted here that 2-D simulation has significant limits with respect to represent the real behavior of ceramic materials. 2-D models have to often simplify the complex crystallographic structure (here closed packed fcc). Also, in 2-D, strengths of local bonds are just averaged as mean value, and with that allow for more available gliding systems of the system than available in reality. In addition, 2-D simulations geometrically involve a lower degree of freedom for deformation than 3-D approaches. Thus, also results from the present 2-D simulations should be interpreted with care for deriving absolute numbers with respect to sizes and velocities. Nevertheless, the simplified 2-D approach should be rather suitable to derive general

trends and possible changes under wide parameter variation, as performed here for velocity and sizes.

The compression MD model setup is presented in Fig. 2(a). The main goals for the compression modeling were (i) mimicking the mechanical properties of TiO$_2$-anatase particles, (ii) studying the influence of particle size under quasi-static loading and (iii) to have a reference system for quasi-static loading conditions and respective deformation patterns. The comparison with the high-velocity impact phenomena could support the assessment of

deformation mechanism in the AD process. The simulations were performed by compressing 2-D single-crystalline particles up to 20% reducing of their initial diameter in Y direction (height reduction). Preliminary simulations demonstrated that such displacement is sufficient to reveal the formation of cracks inside the larger particles. Thus, due to the limited computational time in MD, a compression to a height reduction 20% of the initial particle diameter was applied for the comparative analyses of different sizes. MD compression simulations reported in the
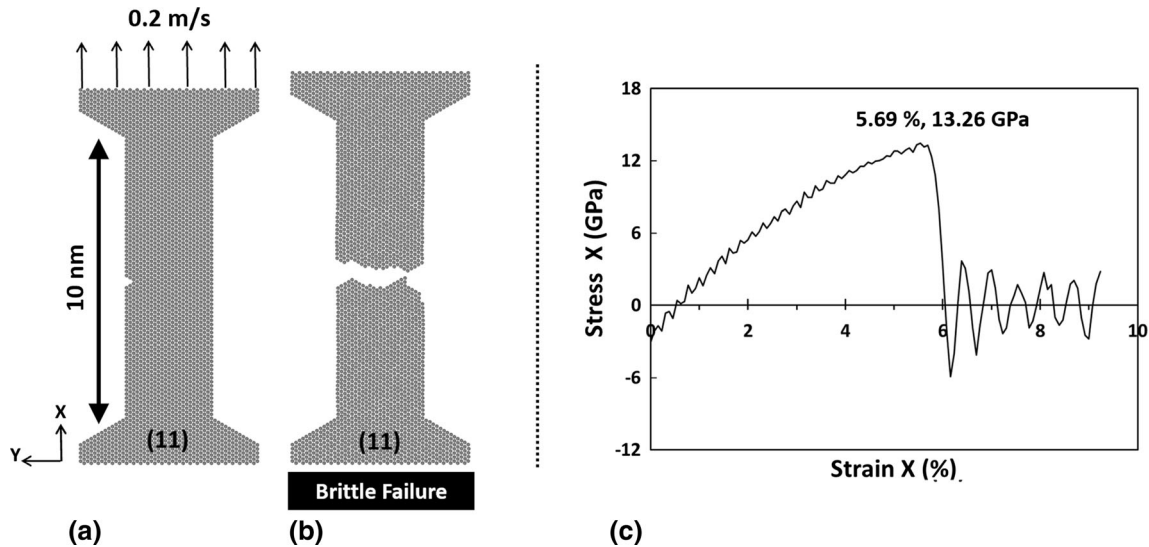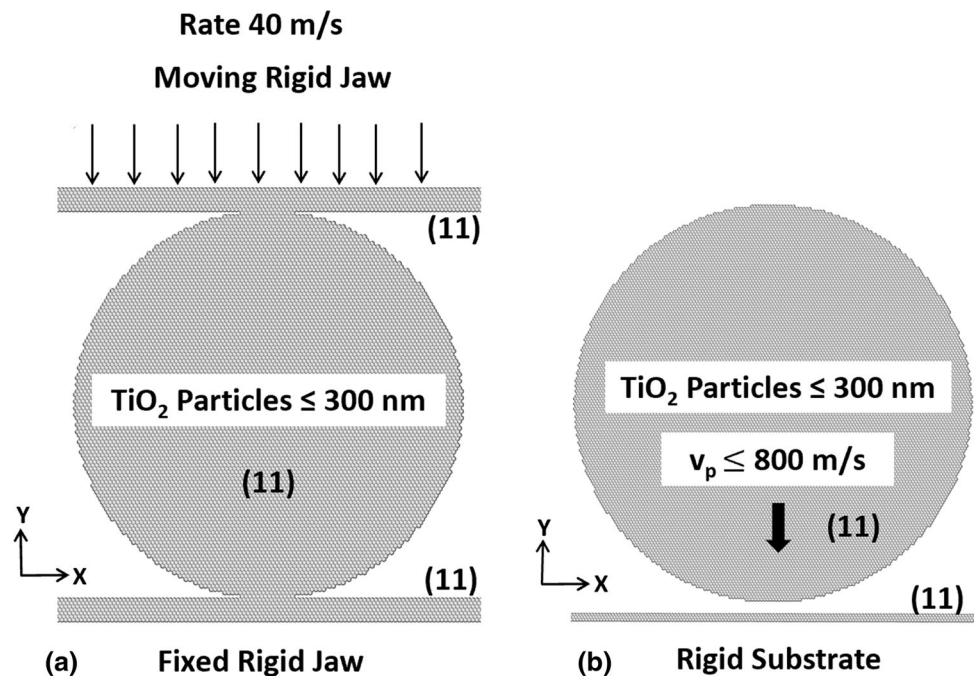

Fig. 1 Principle and output of the MD tensile test model: (a) initial MD tensile test model setup, (b) brittle fracture failure, (c) stress–strain diagram

Fig. 2 Schematics of the MD models for compression and impact simulation: (a) initial setup for the compression models, (b) initial setup for impact models

literature applied compression ratios of 33% for a 50-nm alumina particle (Ref 34) and of 50% for 40-nm Si nanoparticle (Ref 35), respectively. However, the particle sizes in the reported works were far smaller than those applied here in the present study. Similar to the tensile test model, the single-crystalline compression test model was cut from the (11) plane in 2-D, including the 2 rigid jaws at the bottom and top and the particle in between. Accordingly, the crystal orientation of the particle and lower and upper jaws were all the same. The particles were compressed in Y direction between a stationary bottom and a moving upper jaw, the setup being illustrated in Fig. 2(a). The compression simulations were performed for a constant deformation velocity of 40 m/s. Such threshold was set due to restricted computational time in MD, as also stated in previous MD studies of particle compression (Ref 35).

After establishing the material description to match the mechanical properties of TiO_2-anatase, respective models were developed to study the impact behavior of single-crystalline particles in AD with initial diameters of 10, 25, 33, 50, 75, 100 and 300 nm. The particles and substrates were also cut from the (11) plane of atoms in 2-D. The impact models were created according to the setup shown in Fig. 2(b) in order to mimic the AD process parameters by considering particle size and impact velocity as the main variables in simulation. The substrates were considered as rigid for avoiding any influence from substrate deformation and possible boundary effects caused by the model size. The initial particle temperatures were fixed to 300 K. The deformation behaviors of each particle size were studied by varying the impact velocities (Y direction) onto the substrate in a range from 100 to 800 m/s at step widths (accuracy level) of 50 m/s. Only for the size of 75 nm, the step width had to be refined to 10 m/s, to allow for distinguishing transitions in deformation modes.

All tensile, compression and impact simulations were carried out as microcanonical ensemble (NVE), where the total energy and the volume (area in 2-D) of the MD simulation box are considered as constant. The behavior of the system in all of the tensile, compression or impact models, here especially the interaction with the system walls, does not require any definition of periodic boundary conditions. The time steps in all simulations were set to 5×10^{-15} s. Equations of motion were integrated using the Velocity Verlet algorithm (Ref 29). All of the molecular dynamic (MD) simulations were performed by the LAMMPS (https://lammps.sandia.gov) software (Ref 36). The atomic stress and local temperature fields were also calculated by LAMMPS. The atomic strains were calculated by using the OVITO (www.ovito.org) software package (Ref 37). The OVITO software was also applied for visualization of all the morphologies, stress, strain and temperature fields attained by the simulations.

Results

Features of Slow Rate Particle Compression

Slow rate particle compression was simulated for fine tuning of the model to experimental compressive strength data, for studying general features of particle deformation, and to gain information on possible limits with respect to maximum strain before failure. Figure 3(a) to (f) shows the compression behavior by series of time-integrated Von Mises atomic shear strain fields in monolithic TiO_2-anatase particles, with initial diameters of 10, 25, 50, 75, 100 and 300 nm and after final unloading. The particles were all compressed up to 20% of their initial diameters and then unloaded. The Von Mises atomic shear strain field is a useful criterion in atomic simulations showing local regions where inelastic deformation occurs. In other words, shear strain field analyses provide deformation pattern during a loading process and allow to identify regions of locally high or low strain concentrations. Assuming defined strain thresholds for plasticity, the analyses according to Fig. 3 show that traces of similarly high shear strains fields reveal "localized inelastic deformation" mainly occurring along the slip directions of the particular crystal structure. For all the examples of brittle particles with different sizes shown in Fig. 3 under quasi-static compression loads, such "localized inelastic deformation" is observed.

The strain field pattern shows that the "localized inelastic deformation" for all particle sizes starts from the top and the bottom of the particles and then extends towards the center along the slip systems of the close packed (11) planes. In areas closer to the center, the fields of high strain and "localized inelastic deformation," which propagate on different planes towards the center, intersect. Within these areas, a higher density of high strain fields, here denoted as "shear localization," is observed. In these areas of "shear localization," the orientation of maximum strain locally changes, particularly visible for particle sizes $\geq$ 50 nm. As an example, Fig. 3(d) in addition contains a magnified view on such an area of "shear localization." The occurrence of the shear localization causes a change in deformation direction from the slip system towards the maximum shear strain direction of 45°. Such combination of the "localized inelastic deformation" along the slip systems at the initial phase of compression and "shear localization" afterwards can be described as the main compression deformation feature of all investigated particles sizes. Similar analyses of strain pattern were then
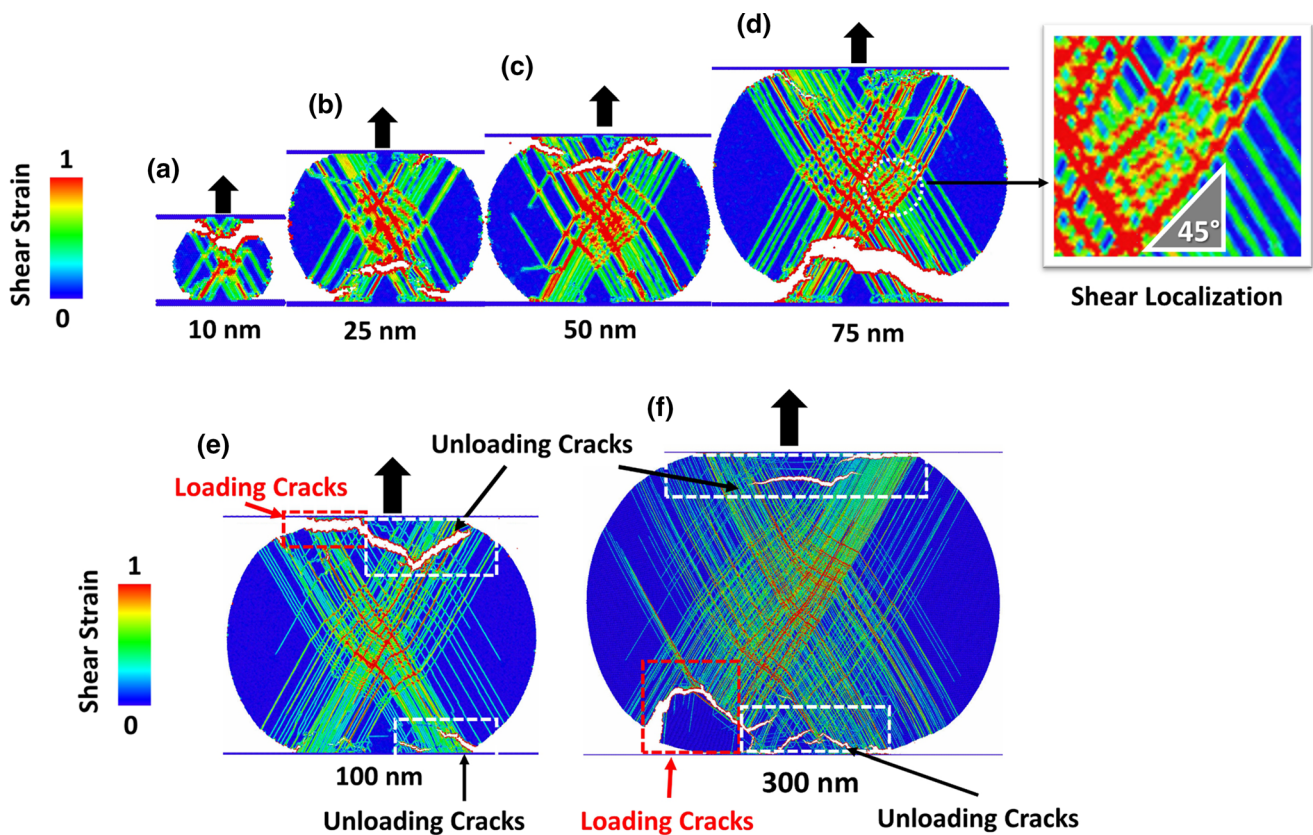
Fig. 3 Simulated deformation patterns after compression loading and unloading (deformation history) by Von Mises shear strain fields inside the TiO$_2$ particles for different initial diameters of (a) 10 nm, (b) 25 nm, (c) 50 nm, (d) 75 nm, (e) 100 nm and (f) 300 nm. The strain pattern reveals (i) localized plastic deformations along the slip systems and (ii) shear localization in an orientation relation of 45° with respect to loading direction

later applied for studying the deformation behavior of the impacted particles.

Apart from the localized deformations and shear localizations observed inside the particles, different types of cracks can be seen in the snapshots of Fig. 3. In particles equal or smaller than 75 nm (Fig. 3a-d), cracks formed only during the unloading phase. These "unloading cracks" are created by the tensile component in the test system when the upper jaw moves back, being still fused to the deformed particle. In larger particles with sizes of 100 nm and 300 nm, however, also cracks are created already during the loading phase, here denoted as "loading cracks" in Fig. 3(e) and (f). With respect to their orientation, these loadings cracks can be associated with shear cracks.

In order to understand the role of particle size during compression, detailed analyses were performed to determine the temporal evolution of stress, strain and temperature fields. For revealing differences of particles that do not show any fracture during the loading phase and others that show loading crack on its outer surface, particle sizes of 50 nm and 100 nm, respectively, were selected as examples.

Figure 4 exhibits the temporal development of stress in Y (parallel to the compression direction), shear strain, temperature and stress in X (perpendicular to the compression direction) in the 50-nm particle during compression with a rate of 40 m/s. Time sequences of 51, 113, 230 and 280 ps were selected in order to illustrate the most important phenomena like stress concentration at contact areas, stress relaxation, localized inelastic deformation and temperature evolution.

As shown in Fig. 4(a), a homogenous stress gradient in Y direction (parallel to the compression direction) develops from the upper and lower contact areas, the maximum stress being more localized at the interface to the upper and lower jaws, respectively. In spite of the continuous compression by upper jaw movement and the increase in contact area to the jaws, local compressive stresses with increasing time show a relaxation that cannot be described by elasticity only. The reason for this stress pattern development is given by the formation of localized inelastic deformations as depicted in the shear strain fields in Fig. 4(b). From comparing the stress in Y direction in Fig. 4(a) with the shear strain fields in Fig. 4(b), it becomes obvious that these inelastic deformations occur locally in
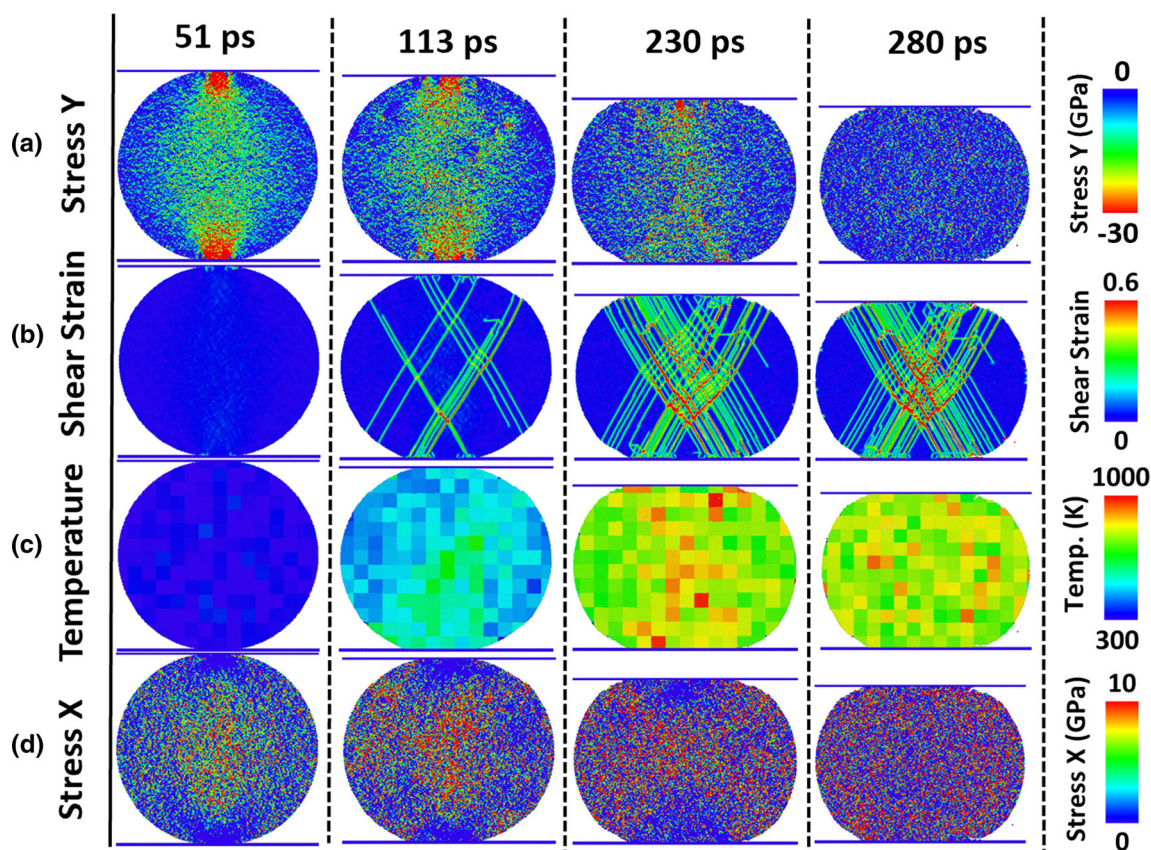
Fig. 4 Temporal development of stress in Y (parallel to compression direction), shear strain, temperature and stress in X (perpendicular to compression direction) inside the 50-nm TiO$_2$ particle during loading with a velocity of 40 m/s at 51, 113, 230 and 280 ps after first contact between jaws and particle. Stress localization and stress release can be clearly seen in the compressive stress results at 51 and 113 ps, respectively. Shear strain fields depict phenomena of "inelastic localized deformation" and "shear localization "at the upper and lower part of the particle (113 ps) and their distribution towards the center of the particle at later time steps (113-280 ps). Local temperatures reveal heat generation in highly deformed zones (113-230 ps), at later time steps also heat diffusion rising the temperature in less deformed areas (230-280 ps). Stress fields in X-direction show an almost homogenous distribution during compression

areas of highest shear stress and that local stress relaxation is associated with the formation of the localized inelastic deformations. Figure 4(b) also indicates that the localized inelastic deformations occur along the slip directions by starting from the contact areas and extending towards the center of the particle. Shear localization can also be observed at time steps of 230 and 280 ps. The local temperature evolution at the time sequences of 51, 113, 230 and 280 ps inside the compressed 50-nm particle is depicted in Fig. 4(c), by analyzing the kinetic energy of atoms in the surrounding of defined atoms. The comparison of the evolution of local temperature fields (Fig. 4c) with that of the strain distribution fields (Fig. 4b) reveals that the particle deformation results in local heat generation associated with inelastic deformation. For the size of 50 nm, a rather homogeneous temperature distribution within the whole particle is achieved at 280 ps (end of the loading phase with 20% displacement in the compression simulation). A peak temperature of 600 K is reached in the 50-nm particle at the end of the loading phase. Even within the

investigated short time scales, heat diffusion seems to play a role, increasing the temperature also in regions that are not or less deformed, finally resulting in a rather uniform temperature distribution.

Figure 5 displays the temporal development of stress in Y (parallel to the compression direction), shear strain, temperature and stress in X (perpendicular to compression direction) in the 100-nm particle during the compression with a rate of 40 m/s. The time steps of 115 ps, 270 ps, 480 ps and 535 ps were selected to reveal the most important phenomena like stress concentration at contact areas, stress relaxation, localized inelastic deformation and especially temperature evolution and crack formation in the 100-nm particle.

According to the stress fields in Y direction in Fig. 5(a), stress concentrations are maximum close to the contact areas to the jaws at a time step of 115 ps. In the next time intervals, the stress fields in Y direction develop patterns of local relaxation and the overall stress then generally declines and vanishes completely at the end of the loading
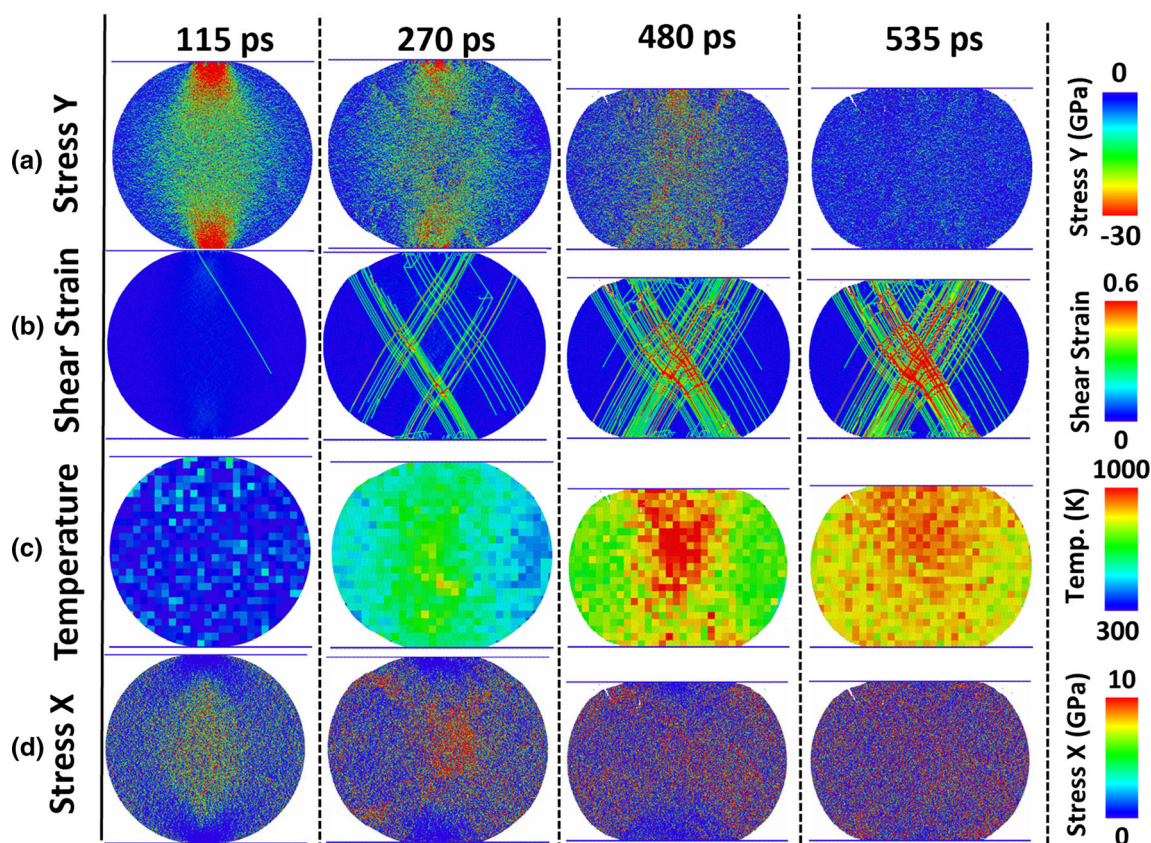
Fig. 5 Temporal development of stress in *Y* (parallel to compression direction), shear strain, temperature and stress in *X* (perpendicular to compression direction) inside the 100-nm TiO₂ particle during loading with a velocity of 40 m/s at 115, 270, 480 and 535 ps after start of the loading. Stress localization and stress release can be clearly seen in the compressive stress results from 270 to 535 ps, respectively. Shear strain fields depict formation of "inelastic localized deformation" and "shear localization "at the upper and lower part of the particle and their distribution toward the center of the particle (270-535 ps). The temperature fields reveal generation of heat in the deformed areas in the upper and center parts (480 ps), and later heat diffusion (535 ps). The particle dimensions are too large for a more homogenous heat distribution during the considered time scales. Stress fields in *X*-direction show an inhomogeneous distribution. The formation of the loading crack in the surface of the particle can be recognized by comparing the development of locally high *X*-stresses at 270 and 480 ps, respectively

phase (535 ps). Like for the 50-nm particle, the locally starting stress relaxation can be explained by inelastic deformation as assessed via shear strain analysis. When the stress concentration in the 100-nm particle peaks at the contact areas to the jaws, the shear strain results in Fig. 5(b) indicate the occurrence of localized inelastic deformations along the slip directions initiating from the contact areas and extending towards the center of the particle. With increasing time, as given by the snapshots at 270 ps and 480 ps after the start of compression, areas of localized inelastic deformation, associated with their intersection, locally change direction from the basic slip system to 45°. The change in strain direction in areas of strain localization becomes more prominent with ongoing deformation, as shown by the snapshots for 480 and 535 ps. The comparison to Fig. 5(a) shows that the development of shear strain fields inside the 100-nm particle correlates well to the decline in Y-stress fields.

The occurrence of localized inelastic deformation inside the particle in Fig. 5(b) generates heat. Figure 5(c) shows the respective temperature fields. The local temperatures are maximum in areas of highest shear concentration close to the center of the 100-nm particle. The maximum temperature within the inelastic deformation areas locally reaches up to 1000 K, despite the superimposed heat diffusion to the surrounding. Within the selected time scales, the generated heat cannot dissipate to a larger volume of the 100-nm particle, thus still remaining rather localized.

As shown in Fig. 5(d), the formation of the loading crack on the surface of the 100-nm particle can be explained by the stress distribution in *X*-direction. At the time step of 270 ps, stress fields in *X*-direction show regions of maximum stress concentration at the upper-left and lower-right surfaces, as well as the center of the 100-nm particle. The formation of the loading crack at the upper-left surface of the 100-nm particle at 270 ps is

associated with this maximum stress concentration in X-direction. Tracing the stress in X-direction at 270 ps and 480 ps also reveals areas of minimum stress concentration close to the interfaces to the upper and lower jaws. This is probably associated with the overall stress compensation by inelastic shear phenomena at the contact area regions, and bonding to the jaws.

In summary, the analyses of temporal development of stress, strain and temperature fields during particle compression provide useful information on phenomena that are associated with particle deformation. The results show that a larger inhomogeneity in stress and strain concentration in larger particles enhances local deformation and possible crack formation.

Figure 6 summarizes the compressive strength/normalized displacement data for the compression simulations of the monolithic TiO_2-anatase particles of different sizes. For all particle sizes, an almost linear regime with the same trend can be recognized up to 5% displacement, associated with the elastic deformation. For all sizes, the trend changes after reaching a maximum compressive stress of about 10-12 GPa, the pressure or stress then decreasing with increasing displacement. This observed strain softening can be attributed to the occurrence of localized inelastic deformation and shear localizations, as described by the shear strain fields depicted in Fig. 3. The deformation by localized inelastic deformation seems to occur stepwise, as indicated by the rather large scatter of stress for increasing displacement, the stress amplitude during this strain softening for small particles being larger than for the bigger ones. From this diagram, a compressive strength of 11 GPa can be derived as the compressive stress of the developed
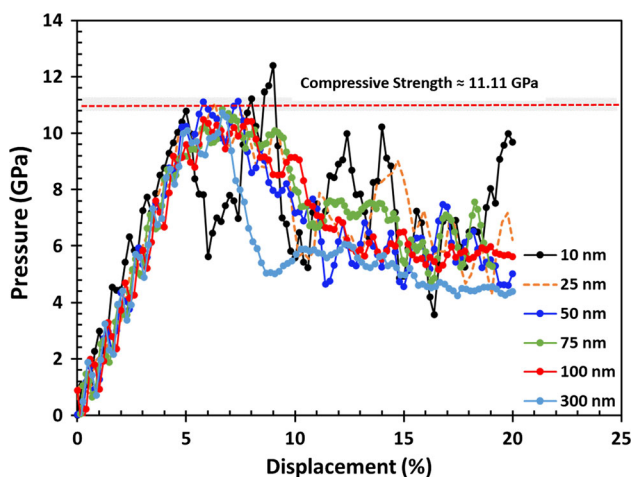

Fig. 6 Calculated compressive strength/normalized displacement relations under compression for different TiO_2 particle sizes ranging from 10 to 300 nm. All particles were compressed to 20% reduction of their initial height. By associated iteration steps, the material model was tuned to match the compressive strength according to experimentally reported data

Lennard-Jones particles, which is in good agreement with the available compressive stress data of 10-12 GPa, reported for single-crystalline TiO_2-anatase particles in the literature (Ref 25, 33).

Features of High-Speed Particle Impacts

Impact Morphologies

This section describes the role of the particle size on particle morphologies for high-speed particle impact during aerosol deposition. Respective analyses were subsequently performed for the range of particles sizes and impact velocities as described by the methods. The simulations show that particle impact results in particular, distinct morphologies, depending on size and velocity. Typical examples of these different morphologies are compared in Fig. 7 for the impacts of a small and a large particle, the selected velocities being typical for the presented phenomena. Figure 7(b), (c) and (d) shows the distinct impact morphologies of a monolithic TiO_2-anatase particle with the initial diameter of 50 nm for impact velocities of 300, 500 and 600 m/s, respectively. Typical impact behaviors and thus morphologies can be distinguished as follows. (i) Rebounding is observed for velocities equal and less than 400 m/s. The particle reverses after impact onto the substrate by back-striking elastic forces between the particle and the substrate. Rebound cracks are formed and seem to be associated with shear crack formation (Ref 38). During rebounding, particles usually keep their original shape, aside some small remains adhering to the substrate. (ii) Bonding behavior is observed for a velocity range from 400 to 500 m/s. Bonding is defined by the whole particle sticking to the substrate. Bonding can be associated with the formation of internal cracks, which do not cause fracture or particle fragmentation under the prerequisite that these internal cracks cannot reach to the outer surface. Then, even crack closure may be observed (Ref 8). During bonding, the particles show substantial flattening by deformation. The observed crack in the bonded particles was mainly perpendicular to the substrate, parallel to the impact direction and created at upper part of the particles which is similar to the configuration of meridional cracks in spherical ceramic particles (Ref 39)—Fig. 7(c). (iii) At velocities higher than 500 m/s, the particle impact behavior is described by fragmentation. Typically, the particle is separated into 3 or more parts upon collision with the substrate. Fragmentation is usually accompanied by flattening and deformation before the first crack appears.

For significantly larger sizes, the velocity ranges and the appearance of impact behaviors differ from those observed for the smaller ones. As examples, Fig. 7(e), (f) and (g) depicts the results on impact morphologies for a TiO_2-
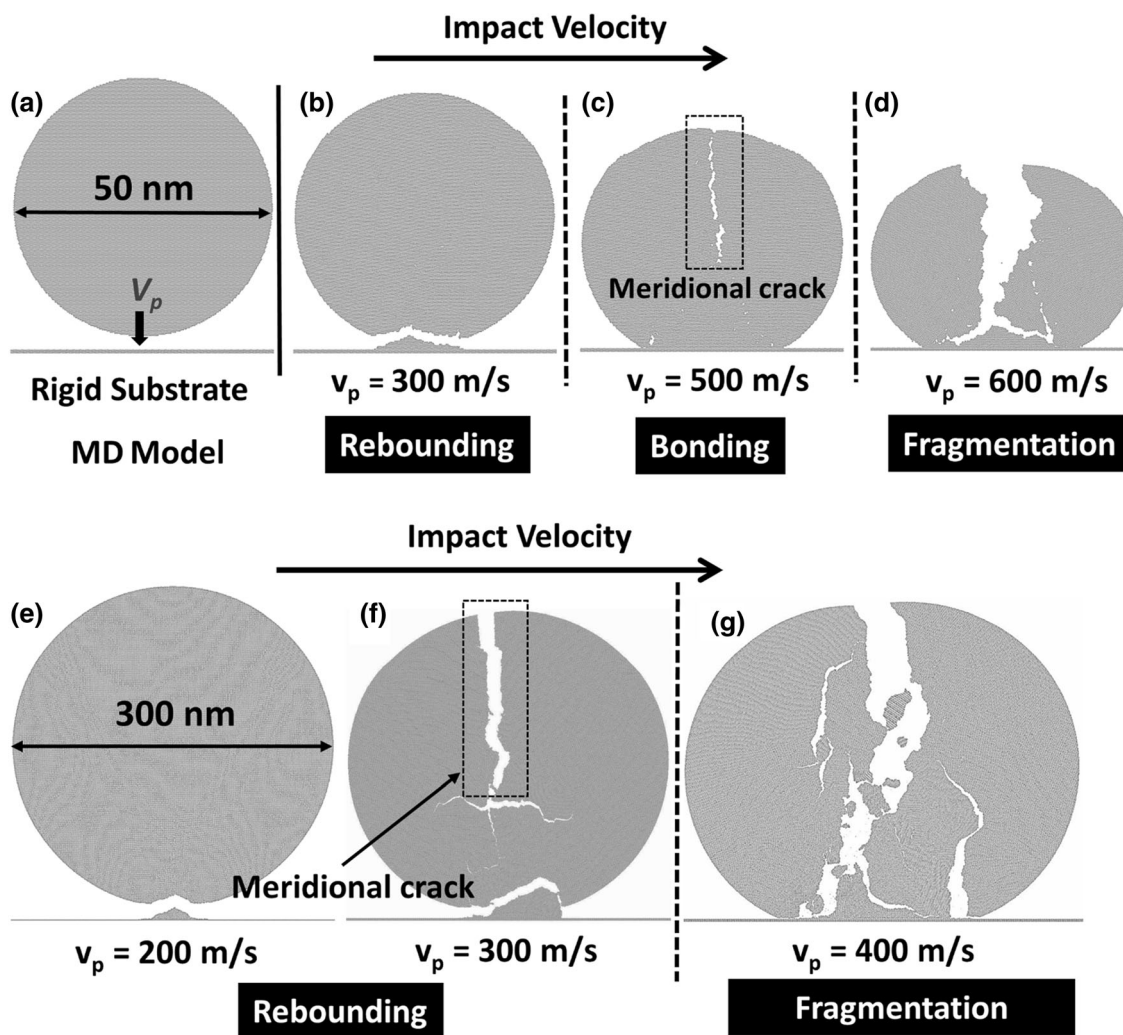
Fig. 7 Impact scenarios as obtained from MD simulations at room temperature as starting condition distinguishing phenomena as (i) rebounding, (ii) bonding and (iii) fragmentation. (a) shows the initial MD impact test setup. Calculated impact morphologies of TiO_2 particles in a size of 50 nm are given for impact velocities of (b) 300, (c) 500 and (d) 600 m/s. Impact morphologies of a particle size of 300 nm are shown for impact velocities of (e) 200, (f) 300 and (g) 400 m/s (g). Three typical impact behaviors of (i) rebounding (b), (ii) full bonding without fragmentation by crack suppression (c) and (iii) partial bonding with fragmentation (d) are observed in the 50-nm TiO_2 particle. For the 300-nm TiO_2 particle, phenomena as (i) rebounding with and without fragmentation (e, f) and (iii) fragmentation (g) can be distinguished

anatase particle with a diameter of 300 nm, travelling at initial velocities of 200, 300 and 400 m/s, respectively. For this size, only two different impact behaviors are observed. (i) Rebounding occurs at impact velocities of less than 400 m/s. However, the rebounding features at 300 m/s of this 300-nm particle are different from those of the small particle, 50 nm in size (compare Fig. 7b with Fig. 7f). In the 300-nm particle, beside the transversal rebounding cracks seen at 300 m/s, in addition, a meridional crack and a longitudinal crack spreading about radially from about the particle center are observed. (ii) The fragmentation behavior in the 300-nm particle occurs at impact velocities equal or higher than 400 m/s. Also features of fragmentation of the larger 300-nm TiO_2-anatase particle (Fig. 7g)

differ from those of the small 50 nm one—Fig. 7(d). For the large particle, beside the first large radial crack, several others develop parallel to the impact direction, resulting in a larger number of fragments. Interestingly, some of these secondary cracks also initiate at the interface to the substrate. In addition, within the fragmentation regime, the larger particle gets less flattened than the smaller one.

Figure 8 summarizes the observed impact behaviors of particles with respect to their size and initial impact velocity. The accuracy of this diagram corresponds to steps in impact velocities of 50 m/s; only for the size of 75 nm, the step width had to be refined to 10 m/s. The transition velocity between the rebounding and bonding behaviors is constant and equal to 400 m/s for nearly all particle sizes.
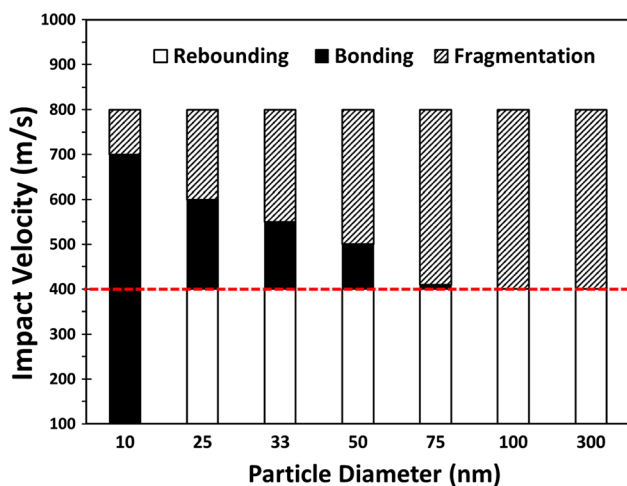
Fig. 8 Impact behavior map for TiO_2 particle of sizes and impact velocities. The accuracy corresponds to steps in impact velocities of 10 m/s for a diameter of 75 nm and 50 m/s for the others

Only for the smallest size of 10 nm, no rebounding behavior could be observed. Concluding from the general trend, the rebounding behavior is not a size-dependent feature, with an exception for very small sizes. The transition velocity between the impact features bonding and fragmentation decreases with increasing particle size, resulting in complete absence of the bonding regime for sizes of 100 nm and 300 nm. This phenomenon could be attributed to the kinetic energy of larger particles that can be high enough to provide the required energy for particle fracture. In addition, fragmentation might be supported by the higher inertia of large particles that locally could be translated into torque and respective stresses. Possible reasons for the size dependence of the bonding and fragmentation behaviors are given in the next section by evaluation of stress, strain and temperature.

Development of Stress, Strain and Temperature

In order to study the size dependency of the bonding and fragmentation behaviors by stress, strain and temperature analysis, distinct particle sizes of 50 and 300 nm were selected. According to Fig. 8, different features for these sizes can be best distinguished at an impact velocity of 500 m/s, the 50-nm particle showing complete bonding behavior, whereas the 300-nm particle is subject to fragmentation. Respective results for the two particle sizes concerning stress, strain and temperature developments are shown in Fig. 9 and 10.

Figure 9 exhibits the temporal development of stress in Y (parallel to the impact direction), shear strain, temperature and stress in X (perpendicular to the impact direction) in the 50-nm particle colliding at the impact velocity of 500 m/s on to the substrate. Time sequences of 5, 10, 25

and 75 ps after initial contact to the substrate are selected in order to illustrate the most important changes in stress concentration at the contact area, stress releasing, localized inelastic deformation and temperature evolution, as well as possible reasons for crack formation. As shown in Fig. 9(a), a homogenous stress gradient in Y direction (parallel to the impact direction) develops from the contact point maximum stress, being more localized at the interface to the substrate. Despite the ongoing compression by particle movement and the increase in contact area to the substrate, local compressive stresses show a relaxation with increasing time, which cannot be explained just by elastic phenomena. The explanation for this stress pattern development is given by the formation of localized inelastic deformations depicted in the shear strain fields in Fig. 9(b). From comparing the stress in Y direction in Fig. 9(a) with the shear strain fields in Fig. 9(b), it becomes obvious that these inelastic deformations occur locally in areas of highest shear stress and that local stress release is associated with the formation of the localized inelastic deformations.

The simulated deformation pattern in the 50-nm particle in Fig. 9(b) is very similar to the presented deformation pattern of the 50-nm particle in the compression simulations (Fig. 3c) concerning features of "localized inelastic deformation" along the slip directions and "shear localization." Within the considered time sequence of Fig. 9(b), the localized inelastic deformation spreads mainly into the lower half of the particle interior. By side branching, the strain distribution and local concentration affect a considerable part of the particle volume, being much less localized at the interface to the substrate.

The local temperature evolution at the time sequences of 5, 10, 20 and 75 ps inside the 50-nm particle is depicted in Fig. 9(c) via analyzing the kinetic energy of atoms in the surrounding of defined atoms. The comparison of the evolution of local temperature fields (Fig. 9c) with that of the strain distribution fields (Fig. 9b) reveals that the particle deformation results in local heat generation associated with inelastic deformation. For the size of 50 nm, a rather homogeneous temperature distribution within the whole particle is attained at 75 ps (end of impact and simulation). Maximum temperatures of only 600 K are reached in the bonded 50-nm particle at an impact velocity of 500 m/s. As mentioned above, even within the investigated short time scales, heat diffusion seems to play a role, leading to a temperature rise also in regions that are not or less deformed, finally resulting in a rather uniform temperature distribution.

Figure 9 also illustrates details of crack formation at the upper part of the 50-nm particle by series of stress fields in X direction in Fig. 9(d). In the selected time sequence, in X-direction, high tensile stresses are created inside the
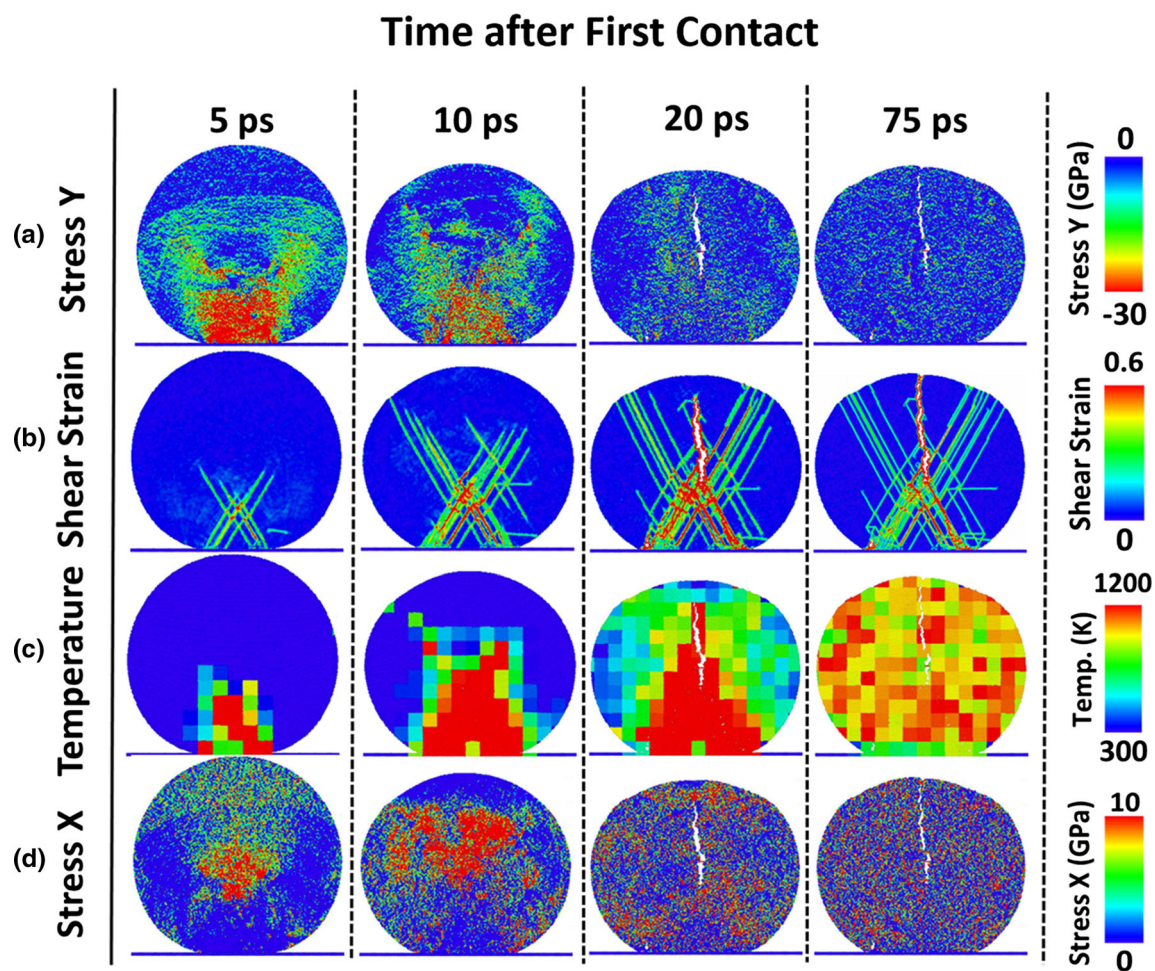
Time after First Contact

Fig. 9 Temporal development of stress in Y (parallel to the impact direction), shear strain, temperature and stress in X (perpendicular to impact direction) inside the 50-nm TiO$_2$ particle during impact with a velocity of 500 m/s at 5, 10, 20 and 75 ps after the first contact to the substrate. Stress localization and stress release can be clearly seen in compressive stress results at 5 and 10 ps, respectively. Shear strain fields depict phenomena of "inelastic localized deformation" and "shear localization "at the lower part of the particle (5 ps) and their distribution toward the center of the particle at later time steps (10-20 ps). Local temperatures reveal a heat generation in highly deformed zones (5-10 ps), at later time steps also heat diffusion rising the temperature in less deformed areas (20-75 ps). Crack nucleation and growth at the upper part of the particle can be explained by stress concentration in X at 10 ps after first contact

particle in the center region and then spread to the upper parts of the particle at already 5 and 10 ps after the contact time. The high stresses in X direction cause crack nucleation and crack growth to the upper part of the particle. Associated with the crack formation, local stresses relax, as seen by the stress field development for times $\geq$ 20 ps after initial contact. It might be worth noting that the crack width decreases for long time scales of 72 ps and that locally even crack closure can be observed.

Figure 10 displays the temporal development of stress in Y (parallel to the impact direction), shear strain, temperature and stress in X (perpendicular to impact direction) in the 300-nm particle colliding with the impact velocity of 500 m/s to the substrate. The time steps of 20, 50 and 80 ps after the first contact to the substrate are selected to reveal the most important phenomena during the collision to the

substrate in order for a deeper understanding of the deformation and the final fragmentation behavior. The velocity of 500 m/s is taken here just as an example in comparison with phenomena in smaller particles showing bonding as described before.

According to the stress fields in Y direction in Fig. 10(a), stress concentrations are maximum close to the contact area to the substrate and at 20 ps after the first contact time and decline with steep gradients to the side (X-direction) and rather homogeneous gradients towards particle center. According to the stress fields in Fig. 10(a), the stress in Y direction is then relaxed at 50 ps and 80 ps mainly in the lower part of the 300-nm particle. As for the small particle described above, the stress relaxation can be explained by inelastic deformation as assessed via shear strain analysis. 20 ps after the first contact, when the stress concentration
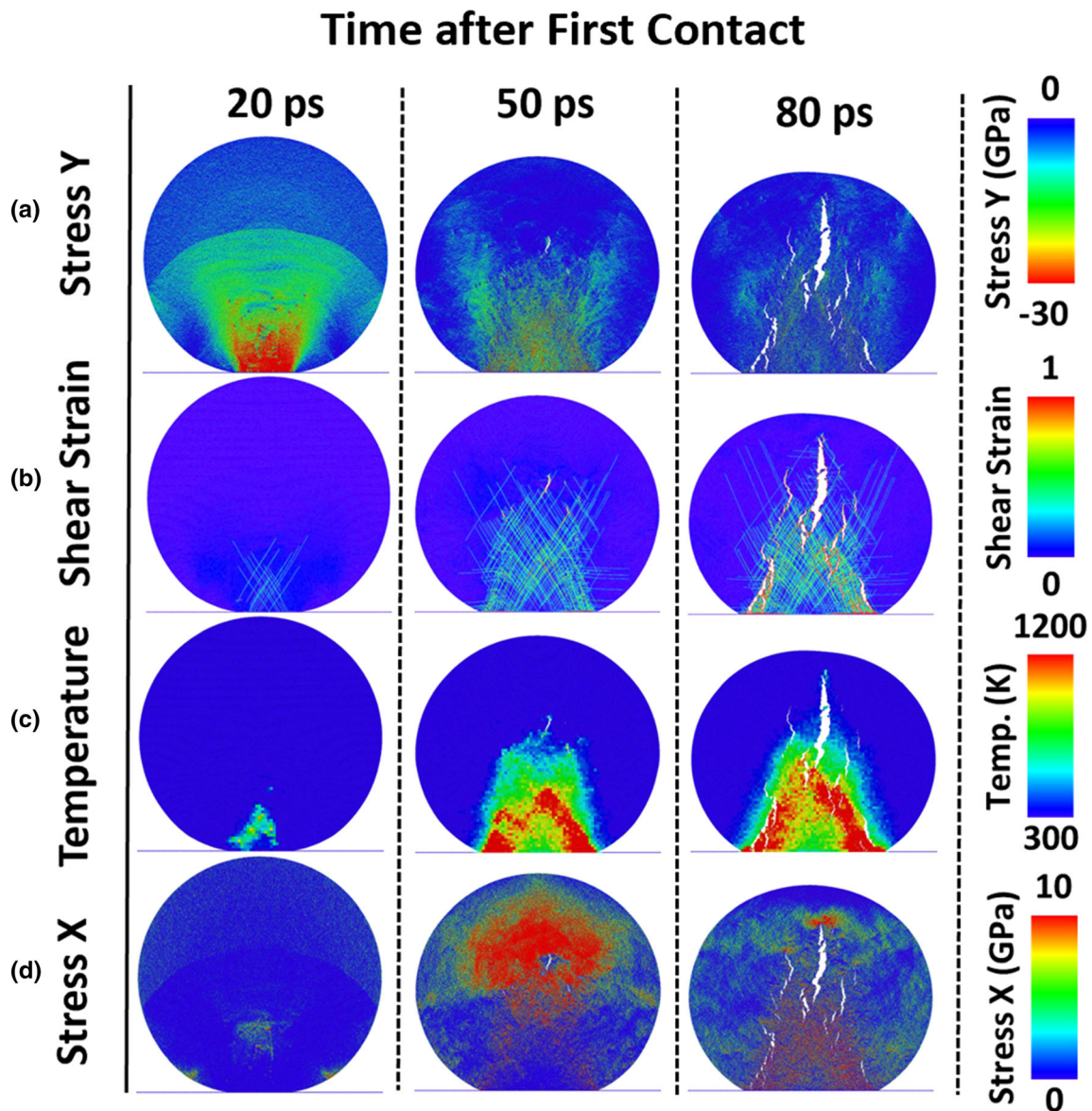
Time after First Contact

Fig. 10 Temporal development of stress in Y (parallel to the impact direction), shear strain, temperature distribution fields and stress in X (perpendicular to impact direction) inside the 300-nm TiO_2 particle during impact with a velocity of 500 m/s at 20, 50 and 80 ps after the first contact to the substrate. Stress localization and stress release can be recognized by comparing stress Y fields at 20 and 50 ps, respectively. Shear strain fields show formation of "inelastic localized deformations" and "shear localization "in the lower part of the particle (20 ps) and their converging distribution mainly within the lower part of the particle (20-80 ps). Temporal temperature fields reveal generation of heat in the deformed areas in the bottom part (50 ps), and only minor, local spread of heat (80 ps). The particle dimensions are too large for more homogenous heat distribution in considered time scales. Fragmentation in the upper part of the particle can be recognized by comparing stress X fields at 50 and 80 ps, consequently

of the 300-nm particle peaks at the interface to the substrate, the shear strain results in Fig. 10(b) already indicate the occurrence of localized inelastic deformations along the slip directions, spreading from the interface to the center of the particle. With increasing time, as given by the snapshots at 50 and 80 ps after the initial contact, areas of localized inelastic deformation then extend laterally at the interface and from the interface towards to the center of the particle, forming a highly deformed cone shape region at

the particle bottom close to the interface. The comparison to Fig. 10(a) shows that the development of shear strain fields inside the particle correlates well to the decline in Y-stress fields. In areas of shear localization, a change in strain spread from slip direction to 45° can be observed.

The occurrence of localized inelastic deformation inside the particle in Fig. 10(b) causes heat generation. Figure 10(c) shows the respective temperature fields. Tracking of local temperatures reveals that local temperatures are

maximum in areas of highest shear concentration. The generated heat within the inelastic deformation cone spreading from the bottom part of the particle inside center increases the maximum temperature locally up to 1200 K. Within the selected time scales, the generated heat does not dissipate to a larger volume of the 300-nm particle, thus still staying rather localized. It should be noted here that the occurrence of shear cracks between time steps of 50 and 80 ps hinders the heat diffusion to areas outside the main deformation cone (see local gradients in X-direction close to the interface to the substrate at 80 ps).

The fragmentation behavior of the 300-nm particle can be explained by the influence of stress in X-direction, as shown in Fig. 10(d). Similar to the small, 50-nm particle, also the large, 300-nm particle shows maximum stress concentration in X direction at the middle and upper parts opposite to the contact area to the substrate. Interestingly, the X-stresses stay rather low in the lower part of the particle, probably associated with the overall stress compensation by inelastic shear phenomena. The initial formation of a mainly radial crack occurs close to the particle center and is associated with a very local relaxation in X-stress. By crack growth, the internally formed radial cracks in the 300-nm particle can reach to the outer surface of the particle and cause fragmentation. As compared to the small particle 50 nm in size, the number of the internal cracks is higher. This can be explained by the steep stress gradients still leaving a high stress concentration in the vicinity of the primary one, all that being attributed to the larger kinetic energy of the large, 300-nm particle and respective translation of momentum into torque by fixed boundary conditions, i.e., limited degrees of freedom for material movement. It may be noted here that the formation of shear cracks only shows minor influence on the development of the X-stress.

For clarifying possible influences, the generation and the diffusion of heat inside the 300-nm particle were analyzed at impact velocities of 100, 300 and 400 m/s at the end of

the simulation. Respective results are shown in Fig. 11. Figure 11(a) shows that at the impact velocity of 100 m/s the temperature does not increase significantly in the 300-nm particle. According to Fig. 11(b), at an impact velocity of 300 m/s, the maximum local temperature reaches about 600 K at the lower part close to the interface to the substrate of the 300-nm particle. As shown in Fig. 11(c), the maximum value of the local temperature at the lower part reaches about 1000 K at an impact velocity of 400 m/s. As most important feature, it should be emphasized that the local temperature rise spreads into a significant amount of the particle volume within the area of the deformation cone. In accordance with Fig. 10(c), locally reached temperatures could be rather high, here possibly enhancing thermally activated processes during the deformation, as enhanced inelastic deformability afterwards.

Discussion

General Deformation and Failure Features

In this MD simulation study, a brittle material with similar mechanical properties to the TiO_2-anatase phase was created by tuning of Lennard-Jones parameters. In order to understand the influence of the particle size and general features in deformation and failure, the slow strain rate compression behavior was modeled for particles with initial diameters of 10-300 nm. The behavior of the TiO_2-anatase particles under compression was then studied by (i) particles morphologies after unloading, (ii) local shear strain distributions and (iii) the compressive stress–displacement results.

By shear strain mapping, fields of localized inelastic deformation and areas of shear localization inside the TiO_2-anatase particles are identified. These features are observed for all particle sizes within the range from of 10
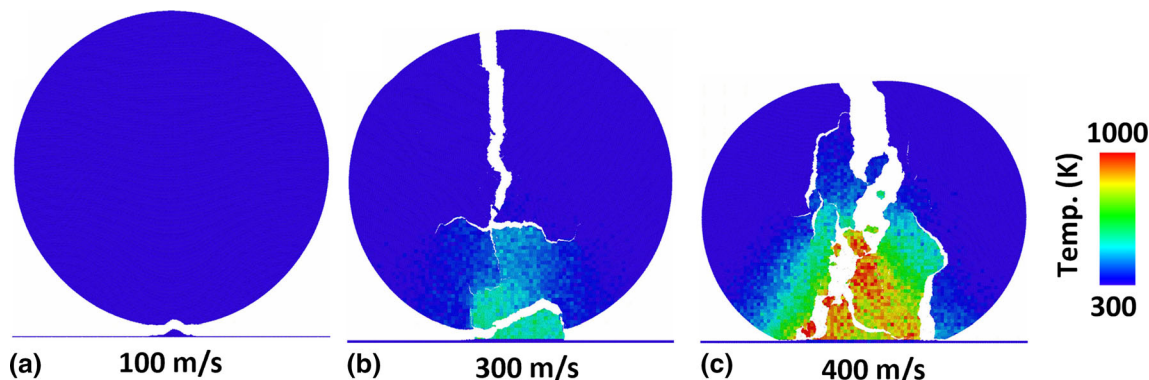

Fig. 11 Heat distribution patterns in the 300-nm TiO_2 particle at different impact velocities of (a) 100 m/s, (b) 300 m/s, (c) 400 m/s at the end of the impact simulation

to 300 nm. The localized inelastic deformation primary occurs along the slip directions of the (11) plane of the closed packed 2-D system. The fields of localized inelastic deformation mainly spread from the interface to the deformation tool towards the particle center. By the intersection of the slip systems shear localization gets prominent, which just means that the amount of deformation is higher inside the particle close to core in comparison with areas close to the interface where the deformation starts. Shear localization can also change the direction of deformation from the slip direction to the maximum shear strain direction of 45°.

The compressive stress/normalized displacement curves for all considered particle sizes show a rather similar behavior in the elastic regime and allow deriving an ultimate compressive stress (UCS) of about 11 GPa. The decline of compressive stress with ongoing deformation after passing the maximum compressive stress indicates strain softening, as usually associated with locally activated failure or deformation as observed for local fracture in composites (Ref 40) or shear banding in metallic glasses (Ref 41), respectively. However, the decline is not continuous, showing significant fluctuations in stress. This can be explained by higher thresholds for the activation of new slip systems for further deformation (Ref 42). The higher amplitude in stress fluctuation for smaller particles is due to the lower number of atoms over which compressive stress is averaged. This could indicate that sizes of active deformation systems or local constraints hindering deformation might be of similar size, independent from particle diameter. In summary, the combination of strain mapping and stress displacement curves under compression indicates that the observed "localized inelastic deformation" can be associated with phenomena like shear banding.

According to the deformation morphologies, particles equal and smaller than 75 nm do not fracture during compression up to a displacement of 20% height reduction of the initial particle diameter. In contrast, larger particles with sizes of 100- and 300-nm particles do show cracks during compression. In these bigger particles, the cracks mainly nucleate at the active slip systems as shear crack, but then later during growth can change direction. Therefore, particle fracture under low strain rate compression of TiO_2-anatase particles is considered as size dependent. This may be attributed to different sizes of crack nuclei depending on system size and thus respective limits to reach overcritical lengths. In detail, the situation will be more complex since also the influence of particle size on local stress states and final stress concentration should be considered. Interestingly, fracture seems to start as mode II, in plane shear, and most prominently respective stress components. However, the formation of loading cracks should not be overinterpreted, since local stress states also depend on the system configuration. In the present compression model, X and thus shear stresses could be enhanced by allowing for rigid contact between particle and jaw atoms.

Despite the simplifications used in modeling and the choice of material system, the present simulation results are in excellent agreement with observed trends in experimental analyses of submicron Al_2O_3-particle compression (Ref 43). Simulation and experiments detect inelastic deformation before failure. The experiments also prove that bigger particles are more prone to crack formation than smaller ones. For both, the modeling results of the present study can provide more information to understand associated phenomena. However, it should be noted that absolute numbers for particle sizes and required stresses are not comparable, due to the simplifications used in present 2-D modeling.

High-Speed Impact Phenomena

The general features observed for quasi-static compression as fields of "localized inelastic deformation" and "shear localization" by the intersection of the slip systems are also found as main impact phenomena in high-speed particle impact. However, due to different loading conditions, overall strain and deformation rates, respective final morphologies differ. The modeling results for TiO_2-anatase particles showed that impact phenomena vary with particle sizes and initial velocities (Fig. 7 and 8). In a velocity range of 100-800 m/s, particles with diameters of 25, 33, 50 and 75 nm show impact behaviors of (i) rebounding, (ii) bonding and (iii) fragmentation. Larger particles with sizes of 100- and 300-nm particles only show (i) rebounding and (iii) fragmentation.

Only for very small particles of 10 nm, no rebounding was observed. Here, the limited amount of overall particle kinetic energy converts to low elastic energy stored in the system, insufficient to exert the required tensile forces for fracture. Aside from that, the transition velocity (Fig. 8) between the rebounding and bonding phenomena of 400 m/s seems to be rather independent of particle size. In contrast, the transition velocity between bonding and fragmentation strongly depends on the particle sizes. The transition velocity between the bonding and fragmentation regions decreases with particle sizes up to 75 nm. The regime for bonding of full particles then vanishes for larger sizes of 100 and 300 nm. This rough classification just describes whether complete particles can stick to the substrate. Details on local microstructure integrity are given by individual crack distributions. Even in the bonding regime, longitudinal or radial cracks can occur. These do not necessarily cause fragmentation, if they do not propagate all the way to the surface (as shown in Fig. 7 for the 50-nm

particles at velocity of 500 m/s). Observed crack lengths and amounts of cracks increase with particle size and can be attributed to local stress states.

A deeper understanding can be achieved by investigating the temporal evolution of stress, strain and temperature fields during the impact (see Fig. 9, 10). Generally, the impact causes Y-stress in particle moving direction rising up at the interface to the substrate, and showing a rather homogeneous decline in direction towards particle center as well as a sharp decrease perpendicular to impact direction. The compressive stress is usually several times greater than the measured compressive stress of the TiO_2-anatase particles determined by the compression test simulations. Thus, the stress concentration is high enough to activate the formation of localized inelastic deformation and shear localization at the lower part of the bonded particles. As a consequence of the stress gradients, the deformation pattern in bonded particles resembles a cone shape pattern, spreading from the interface to the substrate towards the inside of the particle, for simplicity in following termed as "shear cone."

With ongoing deformation, the stress fields show internal patterning. As for particle compression, respective local stress relaxation can be associated with distinct areas of localized inelastic deformation spreading from the interface to the substrate into the particle interior. The associated deformation causes particle flattening. The intersection of these fields of localized inelastic deformation close to the particle's center results in a shear localization, similar to the phenomena observed in particle compression. Also, for the particle impact, in areas of shear localization, a change of shear direction from the slip system to maximum shear stress at 45° could be observed. With ongoing deformation, the area of shear localization spreads with the increase in contact area, and the "shear cone" extends further to the inside of the particle. The deformation mainly occurs in areas of the shear cone and the shear localization inside the particle is probably the major difference to phenomena observed for metallic particles in cold spraying, where most strain occurs directly at the interface to the substrate or to already impacted particles (Ref 6, 7). In comparison with cold spraying, it should also be noted that according to this modeling results, the inelastic deformation in AD is distributed over a larger volume. With overall less inelastic deformation by the different deformation features, this results in locally far less concentrated shear strain than observed in CS.

The occurrence of localized inelastic deformation results in a local temperature rise. By heat diffusion, the temperature can spread over the particle volume even within the very short time scales, at least for the small length scales for particle diameters ≤ 50 nm. For larger particles, where diffusion pathways are longer, the heat remains localized

around the shear cone of highest inelastic deformation between the interface to the substrate and the particle center. In the case of AD of a particle size of 300 nm, areas of shear localization reach temperatures of up to 1200 K. The heat concentration is supported by local cracks hindering diffusion. A locally higher temperature can assist the activation of inelastic deformation and can also assist subsequent fusion and crack closure. Thus, for bigger particles larger areas of shear localization could be expected, as well as a higher amount of areas of localized inelastic deformation.

Particle fragmentation is mainly due to longitudinal or radial cracks caused by X-stresses perpendicular to the impact direction in combination with shear cracks that nucleate at areas of localized inelastic deformation. Both types of stresses are caused by diverting the material flow from impact direction (velocity in Y-direction) to the sides (X, and XY). For bigger particles, the shape adoption in integral involves more atomic displacements in affected regimes than for smaller ones. In addition, the higher inertia of bigger particles is translated to larger parts that change material flow direction and thus cause wider regimes of higher lateral X-stresses than for smaller ones. However, primary cracks only cause a stress relaxation in their close vicinity (see Fig. 9d, 10d). Therefore, the lateral X-stress in the upper regime of the bigger particles is still high and still growing with ongoing deformation, thus enabling the formation of additional cracks causing fragmentation.

Consequences for Coating Formation

Concluding the above discussion for single impacts, the occurrence of cracks determines the deposited particle volume, and the parts that get fragmented and are lost. Only the well bonded volume within or in the vicinity of the shear cone area experiences sufficient localized inelastic deformation, spreading into particle center, and does not contain cracks. However, due to the inelastic deformation, the shear cone volume will contain high amounts of lattice defects. The transition velocity between the bonding and the fragmentation behavior defines the thresholds for crack formation. With respect to particle size effects, these thresholds define conditions for intact shear cone formation. In coating build-up, particles deposited first will be hit by following ones and either being removed completely by high local stresses, or getting fractured along pre-existing cracks, mainly leaving parts of shear cone areas attached to the surface, and in some instances bonding to that. This interpretation for the transition velocity between and fragmentation, and the observed decline of this velocity for larger particles can explain the

experimentally observed minimum particle sizes needed for successful coating formation by AD (Ref 5).

The simplified 2-D model of this study should be sufficient to describe trends for bonding of ceramic particles. However, it would fail to describe real systems for several reasons. One additional degree of freedom for deformation in 3-D allows for different stress states and steeper gradients during impact. The present 2-D analyses are also suffering from a simplified closed packed lattice model. In real 3-D systems, molecular crystal structures would involve less active slip systems for localized inelastic deformation. It may be expected that less slip systems enforce an earlier change in main shear direction towards maximum shear strain. Consequently, this may result in larger amounts of areas inside the particle with highest shear localization and associated grain rotation and grain refinement, as observed in experimental investigations (Ref 1-5). Considering the limits of 2-D analyses, given numbers concerning threshold velocities and particle sizes should be interpreted with care. Thus, the here reported transition to fragmentation and grain refinement might be interpreted as very rough guideline for minimum sizes, than for real deposition experiments with larger particles resulting in coating formation by AD.

Coating deposition occurs under multiple impacts. By impacting secondary particles onto primary ones under whatever lateral offset and velocity, pre-damaged parts in the upper particle region would be prone for failure. Also completely bonded particles that are hit by secondary ones, particularly under lateral offset, will suffer from the complex stress distribution and locally high tensile forces allowing for detachment/erosion.

Despite the limits of 2-D analyses, the present study can provide some information on the interplay between stresses and local strain, and consequences for particle deformation and associated shear cracks as well as radial cracks causing fracture and contribute to a better understanding of particle impact in AD. For smaller particles, associated thresholds for fracture are more difficult to reach, necessitating higher impact velocities. Related to that, the spread of mechanically stable shear cones seems to be an important factor that determines possible particle size effects in AD.

Comparison with Experimental Results

By constraints of computational time, the maximum diameter of particles in the MD modeling was limited to 300 nm. However, the range of the selected particle sizes was wide enough to reveal three different types of impact behavior of TiO_2-anatase particles smaller than 300 nm. For particles equal or larger than 300 nm, only impact behaviors of the types rebounding and fragmentation are expected to happen. Considering that rebounded particles

cannot form AD layers, the modeling results predict that during formation of TiO_2-anatase AD layers in reality, where for example particle sizes of to 2.4 micron are used, only fragmented particles take part in AD layer formation. Therefore, the cone formation by shear deformation can be assumed to play a key role in building up coatings by AD. In fact, formation of AD layers without considering the formation of the cone shape regions remaining after fragmentation on the substrate is meaningless. It is also expected that at high impact velocity, where the kinetic energy of particle is too high, the cone can be destroyed by the kinetic energy of following particles and therefore no AD layers can be formed. The formation of the cones on the surface roughly corresponds to the hammering effect concept (Ref 5), although details on that are sparsely reported. An additional role can be attributed to local temperature rises inside the cone shape regions in large particles. A higher temperature can support deformation and might avoid erosion by following particles.

Bonding Models in AD

As briefly given in Introduction, possible bonding mechanisms for aerosol deposition are mainly distinguished into (i) room temperature impact consolidation (RTIC), which includes particles deformation and fracture during impact (Ref 3, 8, 9), (ii) formation and fusion of new clean fractured surfaces upon impact (Ref 11) and (iii) fragmentation and packing consolidation (Ref 10). In this section, the results of the present study are compared with these three possible explanations for bonding in AD. The main features of the present study are in agreement with the widely accepted description of RTIC (Ref 3, 10, 11, 31, 32). Plastic deformation inside the brittle particles carries out in a very local manner along the slip directions and can even cause shear localization at the intersection of slip directions inside the particle. In fact, in comparison with the previous investigations, the present study can reveal more details about particles deformation in AD and associated basic mechanisms. Previous reports demonstrated that AD is associated with size-dependent features of particle fragmentation (Ref 5, 8, 9). The presented MD simulation results revealed that particle fragmentation is mainly caused by lateral tensile stress (perpendicular to impact direction) resulting in radial cracks in the top part of the particles and by the high shear strains aside the cone regions and possible shear cracks at the lower particle parts. In addition, the present provides information on the influence of particle size on the rebounding behavior, which has not been studied by others so far. In summary, the present MD simulations thus reveal new details concerning regarding the RTIC mechanism in AD.

The presented features during the impact of larger particles correspond to the fragmentation and packing consolidation mechanism presented by Chun et al (Ref 10). According to the MD simulations, the local temperature of particles with sizes of 300 nm or probably larger can rise locally up to 1200 K, which should be sufficient for consolidation. In addition, particle fracture hinders dissipation of the heat to lost parts and thus retains the high temperature inside the remaining cone region on the substrate and might support bonding of following particles in AD.

Concerning the hypothesis of formation and fusion of new clean fractured surfaces (Ref 11), the MD simulations show that for particles equal and smaller than 50 nm, that completely bond to the substrate, partial crack suppression can occur close to the outer top surface—Fig. 7(c). This phenomenon however was never observed for particles larger than 50 nm. Therefore, it is expected that the hypothesis of formation and fusion of new clean fractured surfaces (Ref 11) might be only valid for particles that are too small for practical use in AD due to the deceleration by the bow shock in front of the substrate surface. Whether such mechanisms might apply to individual fragments is not clear yet. However, it must be considered that the velocity of detached parts after fracture is much lower than the original particle velocity and that possible impact angles of fragments are far from optimum.

Conclusion

The results from simplified 2-D MD simulations of 10- to 300-nm TiO_2-anatase particles under compression and impact in aerosol deposition of TiO_2 particles can be summarized as follows:

1. Low strain rate particle compression simulations revealed the occurrence of "localized inelastic deformations" along the slip systems and at areas of their intersection showing "shear localizations." Localized inelastic deformation and shear localization are identified as main deformation phenomena under compression.

2. In particle compression, fracture is size dependant, being more prominent for larger particles.

3. High-speed impact simulations reveal three different impact behaviors of (i) rebounding, (ii) bonding and (iii) fragmentation, depending on particle sizes for small particles. Larger particles only show (i) rebounding and (iii) fragmentation.

4. The transition velocity between rebounding and bonding is nearly independent of particle size. In contrast, the transition velocity between bonding and fragmentation decreases with size.

5. Similar to results from compression, "localized inelastic deformation" and "shear localization" are identified as main deformation features in modeling high-speed impact of the anatase particles. Bonding to the substrate is mainly related to localized inelastic deformation starting at the interface of particles and substrate, and extending as shear cone into the particle interior.

6. Temporal evolutions of field variables as stress, strain and temperature reveal that inelastic deformation and shear localization can locally cause significant temperature rises.

7. Particle deformation is associated with crack formation, cracks being more prominent for larger particle sizes. Crack-free zones are only observed in the shear cone areas, spreading from the particle–substrate interface to center of the particle.

8. Crack-free zones in areas of shear cone formation could be a necessary prerequisite for the formation of layers during AD layers by multiple particle impact.

9. The deformation features of ceramic particles in aerosol deposition are completely different to those in cold spraying of ductile particles. In AD of brittle particles, highly deformed areas spread as shear cone towards particle center, whereas in CS most of the plastic deformation is localized at the interface of the particle to the substrate. Thus, the strain distribution in AD is much less localized than that of CS.

References

1. J. Akedo, Aerosol Deposition Method for Fabrication of Nano Crystal Ceramic Layer, *Mater. Sci. Forum*, 2004, **449–452**, p 43-48

2. J. Akedo, Aerosol Deposition of Ceramic Thick Films at Room Temperature: Densification Mechanism of Ceramic Layers, *J. Am. Ceram. Soc.*, 2006, **89**, p 1834-1839

3. J. Akedo, Room Temperature Impact Consolidation (RTIC) of Fine Ceramic Powder by Aerosol Deposition Method and Applications to Microdevices, *J. Therm. Spray Technol.*, 2008, **17**, p 181-198

4. J. Akedo and M. Lebedev, Microstructure and Electrical Properties of Lead Zirconate Titanate (Pb (Zr$_{52}$/Ti$_{48}$) O$_3$) Thick Films Deposited by Aerosol Deposition Method, *Jpn. J. Appl. Phys.*, 1999, **38**, p 5397-5401

5. D. Hanft, J. Exner, M. Schubert, T. Stöcker, P. Fuierer, and R. Moos, An overview of the Aerosol Deposition Method: Process Fundamentals and New Trends in Materials Applications, *J. Ceram. Sci. Technol.*, 2015, **6**, p 147-182

6. H. Assadi, H. Kreye, F. Gaertner, and T. Klassen, Cold Spraying—A Materials Perspective, *Acta Mater.*, 2016, **116**, p 382-407

7. H. Assadi, F. Gaertner, T. Stoltenhoff, and H. Kreye, Bonding Mechanism in Cold Gas Spraying, *Acta Mater.*, 2003, **51**, p 4379-4394

8. B. Daneshian and H. Assadi, Impact Behavior of Intrinsically Brittle Nanoparticles: A Molecular Dynamics Perspective, *J. Therm. Spray Technol.*, 2014, **23**, p 541-550

9. H. Park, J. Kim, and C. Lee, Dynamic Fragmentation Process and Fragment Microstructure Evolution of Alumina Particles in a Vacuum Kinetic Spraying System, *Scr. Mater.*, 2015, **108**, p 72-75

10. D.M. Chun and S.H. Ahn, Deposition Mechanism of Dry Sprayed Ceramic Particles at Room Temperature Using a Nano-particle Deposition System, *Acta Mater.*, 2011, **59**, p 2693-2703

11. M. Yamada, M.E. Dickinson, K. Shima, N.T. Salim, H. Nakano, and M. Fukumoto, Deposition Behavior and Adhesion Strength of Cold-Sprayed TiO$_2$ Particles, *Proceedings of the International Thermal Spray Conference*, B.R. Marple, A. Agarwal, M.M. Hyland, Y.C. Lau, C.J. Li, R.S. Lima, A. McDonald, Eds., September 27–29, 2011 (Hamburg, Germany), Springer, 2011, p 27–29

12. S. Ravanbakhsh, H. Assadi, H. Nekoomanesh, A. Hassanzadeh, and E. Taheri-Nassaj, Cold Spraying of Ceramic Coatings—A Feasibility Study, *Proceedings of the International Thermal Spray Conference*, B.R. Marple, A. Agarwal, M.M. Hyland, Y.C. Lau, C.J. Li, R.S. Lima, A. McDonald, Eds., September 27–29, 2011 (Hamburg, Germany), Springer, 2011, p 27–29

13. H. Gutzmann, I. Irkhin, F. Gaertner, and T. Klassen, An Experimental Approach to Gain Insight into Cold Spraying of Ceramics, *Proceedings of the International Thermal Spray Conference 2017*, 7-9 June 2017 (Dusseldorf, Germany) (DVS Media GmbH, Curran Associates, Inc., 2017), p 515–517

14. S.D. Johnson, D. Schwer, D.S. Park, Y.S. Park, and E.P. Gorzkowski, Deposition Efficiency of Barium Hexaferrite by Aerosol Deposition, *Surf. Coat. Technol.*, 2017, **332**, p 542-549

15. J. Akedo, Room Temperature Impact Consolidation and Application to Ceramic Coatings: Aerosol Deposition Method, *J. Ceram. Soc. Jpn.*, 2020, **128**(3), p 101-116

16. K. Ma, C.J. Li, and C.X. Li, Narrow and Thin Copper Linear Pattern Deposited by Vacuum Cold Spraying and Deposition Behavior Simulation, *J. Therm. Spray Technol.*, 2020, https://doi.org/10.1007/s11666-020-01102-w

17. J. Exner, M. Schubert, D. Hanft, J. Kita, and R. Moos, How to Treat Powders for the Room Temperature Aerosol Deposition Method to Avoid Porous, Low Strength Ceramic Films, *J. Eur. Ceram. Soc.*, 2018, **39**(2–3), p 592-600

18. H. Kwon, Y. Kim, H. Park, and C. Lee, Impact Behavior for Successful Particle–Particle Bonding in Vacuum Kinetic Spraying, *J. Therm. Spray Technol.*, 2020, https://doi.org/10.1007/s11666-020-01078-7

19. J. Ryu, D.S. Park, B.D. Hahn, J.J. Choi, W.H. Yoon, K.Y. Kim, and H.S. Yun, Photocatalytic TiO$_2$ Thin Films by Aerosol-Deposition: From Micron-sized Particles to Nano-grained Thin Film at Room Temperature, *Appl. Catal. B*, 2008, **83**, p 1-7

20. J. Ryu, B.D. Hahn, J.J. Choi, W.H. Yoon, B.K. Lee, J.H. Choi, and D.S. Park, Porous Photocatalytic TiO$_2$ Thin Films by Aerosol Deposition, *J. Am. Ceram. Soc.*, 2010, **93**(1), p 55-58

21. K. Kendall, Transition Between Cohesive and Interfacial Failure in a Laminate, *Proc. R. Soc. A Math. Phys.*, 1975, **344**, p 287-302

22. K. Kendall, The Impossibility of Comminuting Small Particles by Compression, *Nature*, 1978, **272**, p 710-711

23. E. Calvié, L. Joly-Pottuz, C. Esnouf, P. Clément, V. Garnier, J. Chevalier, Y. Jorand, A. Malchère, T. Epicier, and K. Masenelli-Varlot, Real Time TEM Observation of Alumina Ceramic Nanoparticles During Compression, *J. Eur. Ceram. Soc.*, 2012, **32**, p 2067-2071

24. E. Calvié, J. Réthoré, L. Joly-Pottuz, S. Meille, J. Chevalier, V. Garnier, Y. Jorand, C. Esnouf, T. Epicier, and J.B. Quirk, Mechanical Behavior Law of Ceramic Nanoparticles from Transmission Electron Microscopy In Situ Nano-compression Tests, *Mater. Lett.*, 2014, **119**, p 107-110

25. V. Swamy, A.Y. Kuznetsov, L.S. Dubrovinsky, A. Kurnosov, and V.B. Prakapenka, Unusual Compression Behavior of Anatase TiO$_2$ Nanocrystals, *Phys. Rev. Lett.*, 2009, **103**(075505), p 1-4

26. I. Issa, J. Amodeo, J. Réthoré, L. Joly-Pottuz, C. Esnouf, J. Morthomas, M. Perez, J. Chevalier, and K. Masenelli-Varlot, In Situ Investigation of MgO Nanocube Deformation at Room Temperature, *Acta Mater.*, 2015, **86**, p 295-304

27. F. Östlund, K. Rzepiejewska-Malyska, K. Leifer, L.M. Hale, Y. Tang, R. Ballarini, W.W. Gerberich, and J. Michler, Brittle-to-Ductile Transition in Uniaxial Compression of Silicon Pillars at Room Temperature, *Adv. Funct. Mater.*, 2009, **19**, p 2439-2444

28. W. Kang and M.T.A. Saif, In Situ Study of Size and Temperature Dependent Brittle-to-Ductile Transition in Single Crystal Silicon, *Adv. Funct. Mater.*, 2013, **23**, p 713-719

29. M.P. Allen and D.J. Tildesley, *Computer Simulation of Liquids*, 2nd ed., Oxford University Press, Oxford, 2017

30. K. Hashimoto, H. Irie, and A. Fujishima, TiO$_2$ Photocatalysis: A Historical Overview and Future Prospects, *Jpn. J. Appl. Phys.*, 2005, **44**, p 8269-8285

31. H. Ogawa, Molecular Dynamics Simulation on the Single Particle Impacts in the Aerosol Deposition Process, *Mater. Trans.*, 2005, **46**, p 1235-1239

32. H. Ogawa, Atomistic Simulation of the Aerosol Deposition Method with Zirconia Nanoparticles, *Mater. Trans.*, 2006, **47**, p 1945

33. H. Zhang and J.F. Banfield, Structural Characteristics and Mechanical and Thermodynamic Properties of Nanocrystalline TiO$_2$, *Chem. Rev.*, 2014, **114**, p 9613-9644

34. P. Sarobol, M. Chandross, J.D. Carroll, W.M. Mook, D.C. Bufford, B.L. Boyce, K. Hattar, P.G. Kotula, and A.C. HalRoom, Temperature Deformation Mechanisms of Alumina Particles Observed from In Situ Micro-compression and Atomistic Simulations, *J. Therm. Spray Technol.*, 2016, **25**, p 82-93

35. Y. Hong, N. Zhang, and M.A. Zaeem, Metastable Phase Transformation and Deformation Twinning Induced Hardening-Stiffening Mechanism in Compression of Silicon Nanoparticles, *Acta Mater.*, 2018, **145**, p 8-18

36. S. Plimpton, Fast Parallel Algorithms for Short-Range Molecular Dynamics, *J. Comput. Phys.*, 1995, **117**, p 1-19

37. A. Stukowski, Visualization and Analysis of Atomistic Simulation Data with OVITO—The Open Visualization Tool, *Model. Simul. Mater. Sci.*, 2009, **18**(015012), p 1-7

38. H.A. Carmona, F.K. Wittel, F. Kun, and H.J. Herrmann, Fragmentation Processes in Impact of Spheres, *Phys. Rev. E*, 2008, **77**(5), p 1-10

39. V. Pejchal, M. Fornabaio, G. Žagar, G. Riesen, R.G. Martin, J. Medřický, T. Chráska, and A. Mortensen, Meridian Crack Test Strength of Plasma-Sprayed Amorphous and Nanocrystalline Ceramic Microparticles, *Acta Mater.*, 2018, **145**, p 278-289

40. N. Djordjevic, R. Vignjevic, T. De Vuyst, S. Gemkow, J. Campbell, and K. Hughes, Localization and Damage Induced Softening Using Finite Element and Smooth Particle Hydrodynamic Methods, *J. Serbian Soc. Comput. Mech.*, 2017, **11**(2), p 120-129

41. J.G. Wang, Y.C. Hu, P.F. Guan, K.K. Song, L. Wang, G. Wang, Y. Pan, B. Sarac, and J. Eckert, Hardening of Shear Band in Metallic Glass, *Sci. Rep.*, 2017, **7076**, p 1-10

42. Z.P. Bazant, Z. Bittnar, M. Jirasek, and J. Mazars, *Fracture and Damage in Quasibrittle Structures: Experiment, Modelling and Computer Analysis*, Z.P. Bazant, Z. Bittnar, M. Jirasek, and J. Mazars, Ed., CRC Press, London, 1994, p 259-260

43. S. Kuroyanagi, K. Shinoda, A. Yumoto, and J. Akedo, Size-Dependent Quasi Brittle-Ductile Transition of Single Crystalline Alpha-Alumina Particles During Microcompression Tests, *Acta Mater.*, 2020, **195**, p 588-596